

Deciphering Nickel-catalyzed Electrochemical Ammonia Synthesis from Nitric Oxide

Siwen Zhao

Fudan University

Jiyuan Liu

Nanyang Technological University

Zhibin Zhang

Peking University

Qinghe Wang

Peking University

Chenyuan Zhu

Fudan University

Jing Wu

Fudan University

Chunlei Yang

Fudan University

Guoshuai Shi

Fudan University

Mingwei Chang

Fudan University

Kaihui Liu

Peking University

Shuzhou Li

Nanyang Technological University <https://orcid.org/0000-0002-2159-2602>

Liming Zhang (✉ zhanglm@fudan.edu.cn)

Fudan University <https://orcid.org/0000-0001-6795-3381>

Article

Keywords:

Posted Date: February 8th, 2022

DOI: <https://doi.org/10.21203/rs.3.rs-1313118/v1>

License:  This work is licensed under a Creative Commons Attribution 4.0 International License.

[Read Full License](#)

Abstract

Electrochemical conversion of nitric oxide (NO) to ammonia (NH₃) is a highly attractive route to achieve artificial nitrogen fixation and rebalance the global nitrogen-circle. Yet today's poor mechanistic understanding and unsatisfied selectivity towards NH₃ curtails NOR ecologic prospects. Here, we screened a library of transition metals as electrocatalysts, in which non-noble Ni outperformed others at the top of a volcano-shaped plot. To further elucidate the active motifs, we rationally designed and fabricated five single-crystal Ni foils with various surface orientations as electrocatalysts, and observed higher conversion efficiencies on high-index facets. In particular, Ni(210) demonstrates a unique selectivity towards NH₃ with a yield rate nearly two-folds higher than those of low-index facets. Under the guidance of density functional theory (DFT) calculation, the energy required for key intermediates switching from hollow to bridge sites in the rate-determining hydrogenation step, was established as a descriptor for the capability towards NH₃ production. Our work guides the rational design of NOR electrocatalysts, and more importantly, establishes a paradigm to understand the structure-function correlation in catalysis.

Introduction

Transformations between various nitrogen species are essential for maintaining the global biogeochemical nitrogen cycle^[1-3]. Human activities have led to an anthropogenically induced increasing concentration of atmospheric nitrogen oxides (NO_x), which is harmful to human health and assumed the major responsibility for acid rain formation^[4]. Nitric oxide (NO) is a major component of NO_x in flue gases, and the uptake of NO will further result in an *in vivo* conversion to nitrite^[5], a known carcinogen and one of the main causes for methemoglobinemia. Towards this end, closing the NO-nitrogen cycle is therefore of interest: it is highly desirable to transform NO to harmless or better yet, value-added products.

As an irreplaceable nitrogenous fertilizer, ammonia (NH₃) has been added to agricultural soils to drive global increases in crop yields. Despite of the high efficiency and scalability, the industrial Haber-Bosch process for NH₃ synthesis operates at harsh conditions (300-500 °C, pressure >200 atm), unsustainably employs natural gas as a H₂ feedstock and yields greenhouse gas a byproduct^[6-7]. Alternatively, electrochemical NH₃ synthesis driven by renewable electricity is a sustainable way at ambient conditions and has a great market potential. Dating back to 1960s, electrochemical NH₃ synthesis from N₂ has garnered significant research interest^[8-10], mimicking the biological nitrogen fixation. Major challenges are related to the low activity and selectivity towards NH₃, considering the high energy input required to cleavage N≡N triple bond (941 kJ/mol). Distinguished with the kinetically unfavorable N₂ reduction, electrochemical dissociation of NO is much easier to perform and will potentially address the challenge of low efficiency in nitrogen fixation^[11]. In this regard, electrochemical conversion of NO offers an

appealing One-Stone-Two-Birds direction in alleviating NO accumulation and simultaneously providing valuable chemicals such as NH₃.

Beyond the practical interest, NO is also a key intermediate in nitrogen fixation starting from nitrate^[12-14], in this case, electrochemical NO reduction (NOR) provides an intriguing platform to mechanistically understand and elucidate the intrinsic catalyst structural parameters determining the nature of further reduced products. In contrast to proton reaction, NOR is confirmed to possess multiple reaction pathways, leading to a broad range of reduced nitrogen species, such as nitrous oxide (N₂O), N₂, hydroxylamine (NH₂OH) and NH₃^[15]. Such complexity mainly originates from the multiple electrons transfer steps involved and the strong surface structure sensitivity of the process. To date, electrochemical NOR has been realized on several model systems with variable product distribution^[16-23]. Although N₂ is the thermodynamically favorable product, NH₃ and NH₂OH are more than usually observed, particularly in an acidic electrolyte. Recently, Xiao *et al.*^[18] and Jiao *et al.*^[19] separately demonstrated NO electrochemical conversion on Cu metal with a high selectivity over 90% towards NH₃. Single atom catalysts (SACs) decorated on carbon supports such as Nb-SACs^[20] and Fe-SACs^[21] were reported to majorly produce NH₃ and NH₂OH, respectively. However, enzymatic-inspired catalysts^[22-23], such as heme proteins myoglobin and haemoglobin, primarily catalyze NO to N₂O, although they have structurally similar active sites with Fe-SACs, *i.e.*, Fe-N₄ core. Despite of the initial progresses, searching for a more active and selective catalytic system for NH₃, and more importantly, identifying the intrinsic parameters that govern the product distribution and fixation pathways remain grand challenges in this emerging area.

Herein, we firstly screened a library of transition metals (Ti, V, Cu, Ni, Pd, Pt, Ag and Au) to understand how the electronic structure affects and modulates the product distribution in NOR. Remarkably, we observed an interesting volcano-shaped correlation between calculated nitrogen adsorption free energy and NH₃ production on various transition metals, among which, non-noble metal Ni outperformed others with a 94% selectivity and 9.48 μmol cm⁻² h⁻¹ yield rate towards NH₃. Furthermore, we rationally designed and synthesized five large-area single-crystal Ni foils with various surface orientations to elucidate the structure-function correlation, and observed that the high-index Ni facets exhibit higher selectivities towards NH₃. In particular, Ni(210) achieved 100% selectivity towards NH₃ with a yield rate of 12.02 μmol cm⁻² h⁻¹. Confirmed by density functional theory (DFT) calculations, the abundant steps on high-index facets facilitate to reduce the energy required for the hollow-to-bridge location switch of the key intermediates associated in the rate-determining hydrogenation step, thereby resulting in a higher NH₃ production capability. This work established a benchmark system to study NOR electrocatalysis and setup a paradigm to mechanistically understand the correlation between atomic configuration and catalysis.

Results And Discussion

Comparison of NOR on various transition metals. A suite of transition metals including Ti, V, Cu, Ag, Au, Ni, Pd and Pt were prepared as electrodes (See details in Methods), and the catalytic activity was evaluated in a sulfuric acid-diluted K_2SO_4 (0.5 M, pH=3) aqueous solution under 1 atm of NO in a two-compartment gastight H-cell. Each transition-metal electrode was tested using chronoamperometry at multiple potentials. The gas products were quantified via an on-line gas chromatography (GC), and liquid products were confirmed off-line by three techniques, UV-vis, ion chromatography (IC) and nuclear magnetic resonance (NMR) spectroscopy, for accuracy (see Methods, Supplementary Figures S1-4). Here we should emphasize that the removal of oxygen in electrochemical system is essential to ensure the stability of NO before getting electrochemically reduced on cathode. Otherwise, the residual oxygen will chemically oxidize NO to NO_2 , NO_2^- and finally to NO_3^- , leading to an inflated current density and complex reaction kinetics (Supplementary Figure S5). Beyond product distribution (represented by Faradaic efficiency, FE), we also take emphasis on quantifying product yield rates. To accurately determine the intrinsic activity, the topological surface area (TSA) of electrode was quantified by measuring the topological surface roughness factor (see Methods, Supplementary Figure S6 and Table S1). Figure 1a describes the FEs and yield rates of NH_3 at -0.6 V vs. RHE on different transition metals. Notably, Ni exhibited the highest FE (~94%) and highest yield rate ($9.48 \mu\text{mol cm}^{-2}_{\text{TSA}} \text{h}^{-1}$) towards NH_3 simultaneously. Cu shows a lower FE of 80% with a yield rate of $6.61 \mu\text{mol cm}^{-2}_{\text{TSA}} \text{h}^{-1}$. Instead, the VIII group metal Pd and Pt are more favorable to generate H_2 , having a remarkable decreased NH_3 selectivity of 59% and 51%, respectively. As another competing reaction pathway, NH_2OH was observed with a decent selectivity on some metals, such as Ag, Ti and V. The comparison of activity and selectivity at multiple potentials was summarized in Supplementary Figure S7.

Concurrently, we employed DFT calculations to understand electrochemical NOR. It is confirmed that the adsorption free energy of N (ΔG_{N^*}) is a good descriptor for NH_3 production. Figure 1b demonstrates a volcano-shaped plot between calculated ΔG_{N^*} and NH_3 production (shown by both FE and yield rate) on various transition metals. The ΔG_{N^*} of Ni is close to the optimal value, neither too strong nor too weak. Accordingly, Ni exhibited simultaneously the highest FE and highest yield rate towards NH_3 . As the adjacent transition-metal to Ni, Cu exhibits a weaker N adsorption, thus a lower FE and production rate. The poor performance of metal Pd and Pt is due to their remarkable capability to generate H_2 [24–25], which is a major competing reaction to produce NH_3 . Moreover, Ti, V, Ag and Au show much lower selectivities and production rates because of large deviations from the optimal value of ΔG_{N^*} .

To further understand the activities and selectivities of these transition metal electrodes, the electrochemical process of NOR were theoretically investigated on the most stable facets of various transition metals (see Methods, Supplementary Figure S8). After screening possible NOR pathways, two feasible ones, O^* and N^* pathways, were proposed as listed in Supplementary Table S2. Rather than directly dissociating into atomic O^* and N^* , the NO molecule forms adsorbed NHO^* (O^* pathway) or NOH^* (N^* pathway) intermediate at the hollow site of metal atoms through an associative pathway [16]. Regardless of each pathway, the adsorption energies of intermediates involved in the rate-determining

steps (RDS), $\text{NO} \rightarrow \text{NHO}^*$ for O^* pathway and $\text{NH}^* \rightarrow \text{NH}_2^*$ for N^* pathway, depend almost linearly on ΔG_{N^*} due to the scaling relation (Supplementary Figure S9), which can well explain the remarkable correlation between ΔG_{N^*} and NH_3 production.

Design and fabrication of single-crystal Ni foils. To understand the active site motifs of Ni towards NOR, we rationally designed monocrystalline Ni with well-defined lattices as electrocatalysts. According to the Miller indices $\{hkl\}$, Ni facets can be classified into low-index facets including $\{100\}$, $\{111\}$ and $\{110\}$, and high-index facets which constitute terraces, steps and/or kinks with variable orientations. A general microfacet notation for cubic structure has been proposed by Somorjai in 1980 [26], in which each high-index facet can be described by a combination of low-index facets with different constitution ratios. For example, Ni(210) is denoted as Ni(S)-[$1_1(110)+1_1(100)$], indicating that one-atom-wide (100) terraces are separated by one-atom-wide (110) steps. Likewise, Ni(310), denoted as Ni(S)-[$1_1(110)+2_2(100)$], can be visualized as a kinked surface with a repetitive unit having two-atom-wide (100) terraces and one-atom-wide (110) steps. The presence of low-index terraces/steps suggests a high degree of site heterogeneity on high-index facets, which can be clearly observed in the side view of Ni(210), where the kinks are shown to have atomic sites with six-(pink), nine-(yellow) and eleven-(blue) fold coordination (Figure 2a). To elucidate the structure-function correlation, we rationally prepared five single-crystal Ni facets with distinct coordination environments and site motifs, including two low-index facets, *e.g.*, Ni(100) and Ni(111), and three high-index facets, *e.g.*, Ni(210), Ni(310) and Ni(520). Those high-index facets can be denoted as different combinations of low-index facets, and are located on the inverse pole figure as shown in Supplementary Figure S10.

The growth of single-crystal Ni follows our recently developed “seeded abnormal grain growth” technique [27]. Figure 2b shows an optical image of a large-format single-crystal Ni foil with (111) facet, the crystal orientation of which is corroborated by the low energy electron diffraction (LEED) (Figure 2c). The uniform color contrast of five single-crystal Ni foils shown in electron-back scattered diffraction (EBSD) at the micro-meter scale strongly suggests the absence of *in-plane* misorientation on surface (Figure 2d). X-ray diffraction was engaged to track the crystallinity of bulk Ni foils. As shown in Figure 2e, XRD symmetric scans confirm the single crystallinity nature of fcc Ni foils textured in five *out-of-plane* directions, which are in good agreement with EBSD mappings. On the whole, these characterizations proved that the synthesis of single-crystal Ni is atomically controllable.

Understanding NO-to-NH₃ conversion on Ni. The electrochemical performance of single-crystal Ni was evaluated under the identical condition as we described above. Selectivity and yield rate on five single-crystal Ni facets were plotted as a function of applied potential, as summarized in Figure 3a and Supplementary Figure S11. Remarkably, NH_3 is the major product on monocrystalline Ni at a more positive bias. The hydrogen evolution reaction (HER), as a major competing reaction, was gradually dominant as the applied potential increased negatively from -0.8 V to -1.0 V vs. RHE, due to the mass transfer limitation of NO (solubility ~ 1.94 mM at 25 °C) [28] under a large electrochemical polarization. In the medium potential region, NOR kinetically dominates the reaction. To exclude the influence from mass

transport, we focused on the medium potential region to understand NOR. As shown in Figure 3a, all high-index Ni facets explicitly demonstrate higher selectivity towards NH_3 . In particular, Ni(210) achieved almost a unique selectivity with a yield rate nearly two-folds higher than those of Ni(100) and Ni(111) (Supplementary Figure S11). It is worth to note that the facet orientation of all selected single-crystal Ni foils remained stable after electrochemical NOR, confirmed by EBSD characterization (Supplementary Figure S12).

We performed DFT calculations to understand the activities on various Ni facets, including both N^* pathway ($\text{NO} \rightarrow \text{NOH}^* \rightarrow \text{N}^* + \text{H}_2\text{O}$, $\text{N}^* \rightarrow \text{NH}^* \rightarrow \text{NH}_2^* \rightarrow \text{NH}_3$) and O^* pathway ($\text{NO} \rightarrow \text{NHO}^* \rightarrow \text{NH}_2\text{O}^* \rightarrow \text{NH}_3 + \text{O}^*$, $\text{O}^* \rightarrow \text{OH}^* \rightarrow \text{H}_2\text{O}$)^[18]. DFT results suggest that N^* pathway with $\text{NH}^* \rightarrow \text{NH}_2^*$ as the RDS dominates NOR on Ni(111), Ni(100), Ni(310) and Ni(520) facets (see Supplementary Figures S13-14 and Table S3 for adsorption energies of all intermediates), and the energy increase associated with RDS are 0.16, 0.33, 0.10, and 0.09 eV, respectively (Figure 3b). Since the stepped surface Ni(310) and Ni(520) demand less energy than that of flat surface Ni(100) and Ni(111), they would exhibit better NH_3 production performances, which is in-line with the experimental results in Figure 3a. For Ni(210), both N^* and O^* pathway were plotted in Figure 3c. Although the N^* pathway exhibits a fairly smaller barrier of 0.07 eV, the O^* pathway is energetically preferred on Ni(210) as it shows a continuous downhill conversion, which can well explain its best performance towards NH_3 production in experiment.

We also observed a switch of adsorption sites for intermediates in the RDS of N^* pathway on all involved facets. DFT calculations show that the first three generated species, NOH^* , N^* and NH^* , prefer to occupy a hollow active site, the NH_2^* intermediate, instead, is only stabilized at a bridge site. Therefore, the adsorption site has to switch from a hollow to a bridge site at the step of $\text{NH}^* \rightarrow \text{NH}_2^*$. It is presumable that the free energy demanded for such switch, denoted as ΔG_s , may determine the activity towards NH_3 production. Figure 3d plotted the NH_3 yield rate in log scale as a function of ΔG_s on Ni(111), Ni(310), Ni(210) and Ni(520), which demonstrates an roughly exponential correlation. As for Ni(210), although it favors O^* pathway, the hydrogenation of O^* to produce OH^* similarly associates with a location switch from hollow to bridge site, which is exothermic considering the energetic downhill nature of O^* pathway on Ni(210). In this regard, ΔG_s can be regarded as 0 eV on Ni(210). Surprisingly, the ΔG_s of O^* pathway on Ni(210) appears along the trend line in Figure 3d, suggesting ΔG_s is a reasonable theoretical parameter to describe the yield of NH_3 . Such correlation can be well explained from a view of geometric structure. Ni(100) displays the largest ΔG_s as the coordination number of NH^* has to decrease from four (hollow site) to two (bridge site) associated with its hydrogenation. Instead, the NH^* coordination only need to drop from three (hollow site) to two (bridge site) at the closely-packed Ni(111) surface, which exhibits a smaller ΔG_s in relative to Ni(100). For high-index Ni facets, the adsorption capability of bridge site will be strongly elevated because of the abundant undercoordinated step sites, which effectively reduce the required ΔG_s and ultimately accelerate the yield of NH_3 .

Conclusion

To conclude, we demonstrate a volcano-shaped correlation between calculated nitrogen adsorption free energy and NH_3 production on various transition metals, and screened out Ni to be the most active catalyst for electrochemical NO-to- NH_3 conversion. To gain deep insight in such conversion, we rationally designed and fabricated large-area single-crystal Ni foils with various surface orientations, and achieved ~100% selectivity of NH_3 on Ni(210) facet. DFT calculation revealed the RDS of NOR on Ni associated with a hollow-to-bridge location switch of intermediate, and the energy required in this step is demonstrated as a descriptor for the yield of NH_3 . Our results demonstrate a benchmark system for NOR electrocatalysis, and provide an important mechanistic insight that could further guide the rational design and optimization of Ni-based NOR catalysts.

Associated Contents

Supporting Information. Methods, Supplementary figures and tables are included in Supporting Information. The quantification of liquid and gas products, calculation energy diagrams and adsorption energies of all intermediates, high- and low-index Ni facets and their electrochemical NOR results.

Declarations

AUTHOR INFORMATION

Corresponding Author

*Email: zhanglm@fudan.edu.cn; lisz@ntu.edu.sg

Author Contributions

L.Z. designed and conceived the experiment. S.Z., C.Z., C.Y., J.W. G.S. and M.C. characterized the electrodes and performed electrochemical characterization as well as data analysis. J.L. and S.L. worked on DFT calculations. Z.Z, Q.W. and K.L. carried out the synthesis of monocrystalline Ni electrodes, and performed EBSD, XRD and LEED characterizations. All authors discussed the results and participated in writing the manuscript.

NOTES

The authors declare no competing financial interest.

ACKNOWLEDGMENT

This research was supported by National Natural Science Foundation of China (Grants 21872039, 22072030 and 52025023), Science and Technology Commission of Shanghai Municipality (Grants 18JC1411700 and 19DZ2270100), The Key R&D Program of Guangdong Province (Grant 2020B010189001). L.Z. thanks funding support from the original personalized project of Fudan

University. S.L. thanks funding support from Singapore Academic Research Fund Tier 1 (RG8/20 and RG10/21). C.Z thanks funding support from China Postdoctoral Science Foundation (2021M700810).

References

1. Bolle, H. J. et al. The natural environment and the biogeochemical cycles. *Eds. Springer. Berlin Heidelberg: Berlin, Heidelberg.* pp 61-81 (1982).
2. Canfield, D. E., Glazer, A. N. & Falkowski, P. G. The evolution and future of earth's nitrogen cycle. *Science* **330**, 192–196 (2010).
3. Chen, J. G. et al. Beyond fossil fuel-driven nitrogen transformations. *Science* **360**, eaar6611 (2018).
4. Gerhardsson, L. et al. Chapter 15 - Effects of acid precipitation on the environment and on human health. In *advances in environmental control technology: health and toxicology. Eds. Gulf Professional Publishing: Burlington.* pp 355-364 (1997).
5. Liou, G.Y. & Storz, P. Reactive oxygen species in cancer. *Free Radic. Res.* **44**, 479–496 (2010).
6. Lehnert, N. et al. Reversing nitrogen fixation. *Nat. Rev. Chem.* **2**, 278–289 (2018).
7. Kandemir, T. et al. The Haber–Bosch process revisited: on the real structure and stability of “ammonia iron” under working conditions. *Angew. Chem. Int. Ed.* **52**, 12723–12726 (2013).
8. Licht, S. et al. Ammonia synthesis by N₂ and steam electrolysis in molten hydroxide suspensions of nanoscale Fe₂O₃. *Science* **345**, 637–640 (2014).
9. Foster, S. L. et al. Catalysts for nitrogen reduction to ammonia. *Nat. Catal.* **1**, 490–500 (2018).
10. Bao, D. et al. Electrochemical reduction of N₂ under ambient conditions for artificial N₂ fixation and renewable energy storage using N₂/NH₃ Cycle. *Adv. Mater.* **29**, 1604799 (2017).
11. Hara, K. et al. Electrocatalytic reduction of NO on metal electrodes and gas diffusion electrodes in an aqueous electrolyte. *J. Electroanal. Chem* **451**, 181–186 (1998).
12. Duca, M. & Koper, M. T. M. Powering denitrification: the perspectives of electrocatalytic nitrate reduction. *Energy Environ. Sci.* **5**, 9726–9742 (2012).
13. Chen, G. F. et al. Electrochemical reduction of nitrate to ammonia via direct eight-electron transfer using a copper–molecular solid catalyst. *Nat. Energy.* **5**, 605–163 (2020).
14. Li, J. et al. Efficient ammonia electrosynthesis from nitrate on strained ruthenium nanoclusters. *J. Am. Chem. Soc.* **142**, 7036–7046 (2020).
15. Katsounaros, I. et al. Structure- and coverage-sensitive mechanism of NO reduction on platinum electrodes. *ACS Catal.* **7**, 4660–4667 (2017).
16. Clayborne, A. et al. Elucidation of pathways for NO electroreduction on Pt(111) from first principles. *Angew. Chem. Int. Ed.* **54**, 8255–8258 (2015).
17. Chun, H. J. et al. Atomistic insights into nitrogen-cycle electrochemistry: A combined DFT and kinetic Monte Carlo analysis of NO electrochemical reduction on Pt(100). *ACS Catal.* **7**, 3869–3882 (2017).

18. Long, J. et al. Direct electrochemical ammonia synthesis from nitric oxide. *Angew. Chem. Int. Ed.* **59**, 9711–9718 (2020).
19. Ko, B. H. et al. Electrochemical reduction of gaseous nitrogen oxides on transition metals at ambient conditions. *J. Am. Chem. Soc.* **144**, 1258–1266 (2022).
20. Peng, X. et al. Ambient electrosynthesis of ammonia with efficient denitration. *Nano Energy* **78**, 105321 (2020).
21. Kim, D. H. et al. Selective electrochemical reduction of nitric oxide to hydroxylamine by atomically dispersed iron catalyst. *Nat. Commun.* **12**, 1856 (2021).
22. Pan, K.C. et al. Electrocatalytic reactions of nitric oxide on prussian blue film modified electrodes. *J. Electroanal. Chem.* **501**, 160–165 (2001).
23. Bedioui, Z. F. Electrocatalysis of nitric oxide reduction by hemoglobin entrapped in surfactant films. *Electrochem Commun.* **3**, 435–438 (2001).
24. Janssen, L. J. J., Pieterse, M. M. J. & Barendrecht, E. Reduction of nitric oxide at a platinum cathode in an acidic solution. *Electrochim. Acta.* **22**, 27–30 (1977).
25. de Vooy, A. C. A. et al. Mechanistic study on the electrocatalytic reduction of nitric oxide on transition-metal electrodes. *J. Catal.* **202**, 387–394 (2001).
26. Van Hove, M. A. & Somorjai, G. A. A new microfacet notation for high-Miller-index surfaces of cubic materials with terrace, step and kink structures. *Surf. Sci.* **92**, 489–518 (1980).
27. Wu, M. et al. Seeded growth of large single-crystal copper foils with high-index facets. *Nature* **581**, 406–410 (2020).
28. Kim, D. et al. Unveiling electrode-electrolyte design-based NO reduction for NH₃ synthesis. *ACS Energy Lett.* **5**, 3647–3656 (2020).

Figures

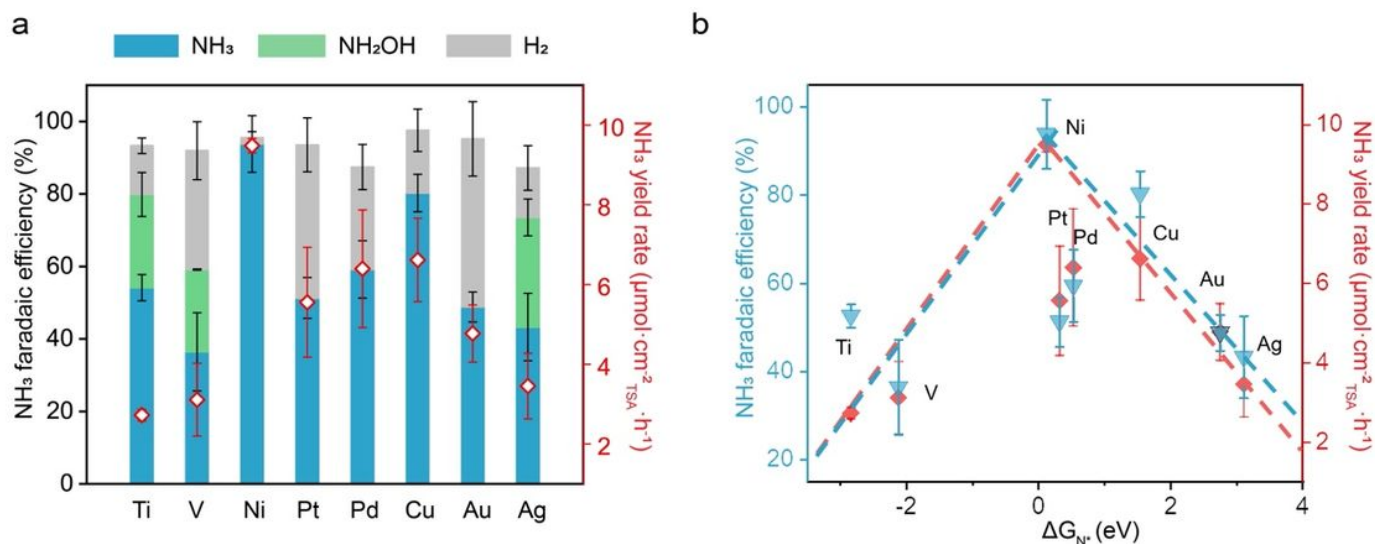


Figure 1

Distinguished NO-to-NH₃ conversion on various transition metals. (a) FE (bar) and NH₃ yield rate (rectangle, normalized by the topological surface area, TSA) at -0.57 V vs. RHE. (b) Volcano-shaped correlation of ΔG_N^* with FE and yield rate of NH₃. All the activity measurements were performed in a NO-saturated sulfuric acid-diluted K₂SO₄ (0.5 M, pH=3) aqueous solution, and the error bars represent the standard deviation of triplicate measurements.

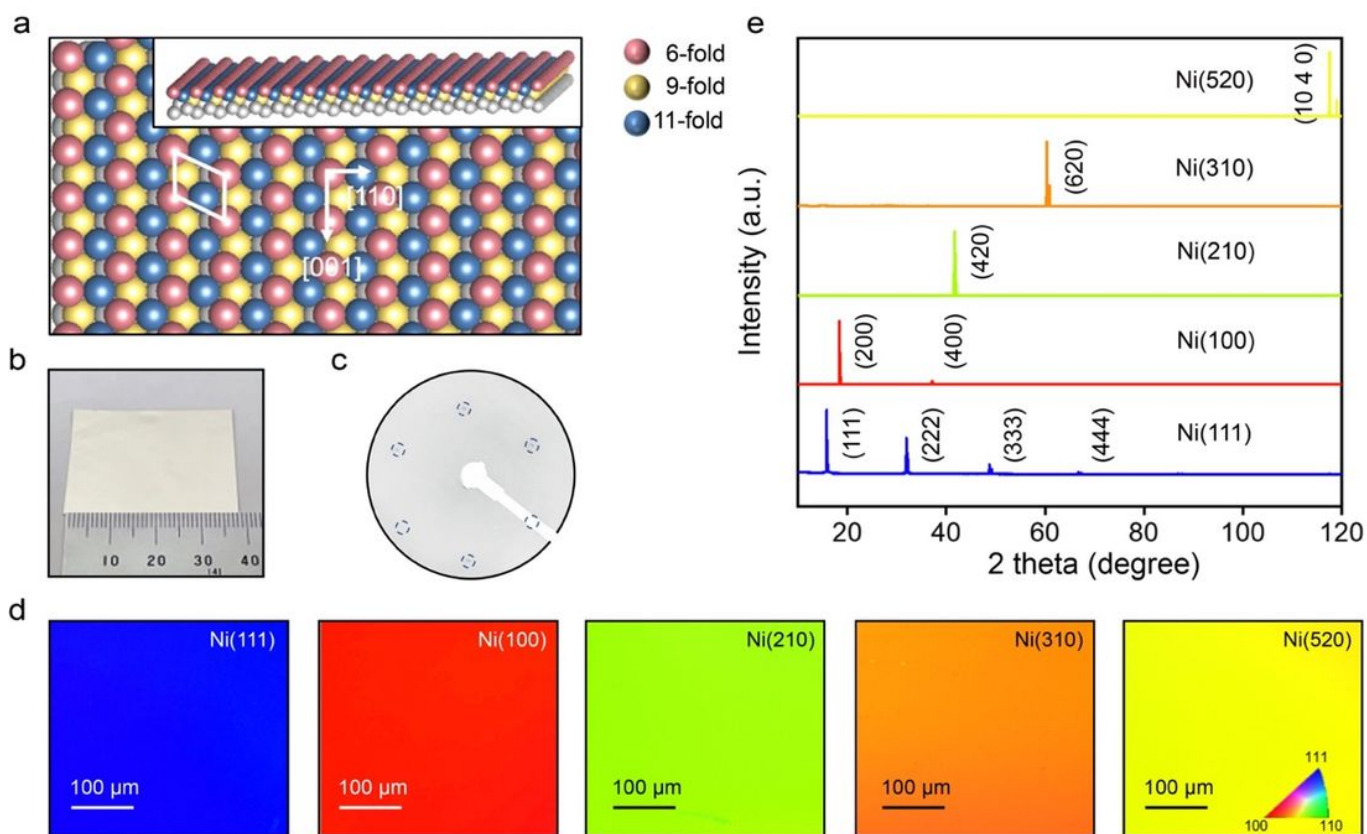


Figure 2

Large-area single-crystal Ni foils. (a) A schematic illustration of high-index single-crystal Ni(210) facet having surface atoms with distinct coordination environments. The side-view is shown as an inset. The coordination numbers of the unsaturated Ni atoms are: six (pink), nine (yellow) and eleven (blue). (b-c) A digital photograph of a large-area single-crystal Ni(111) foil (b) and the representative LEED image (c). (d) Large-area EBSD mapping on various as-prepared Ni facets. (e) Representative XRD 2 theta-scan of single-crystal Ni foils measured by Ag target.

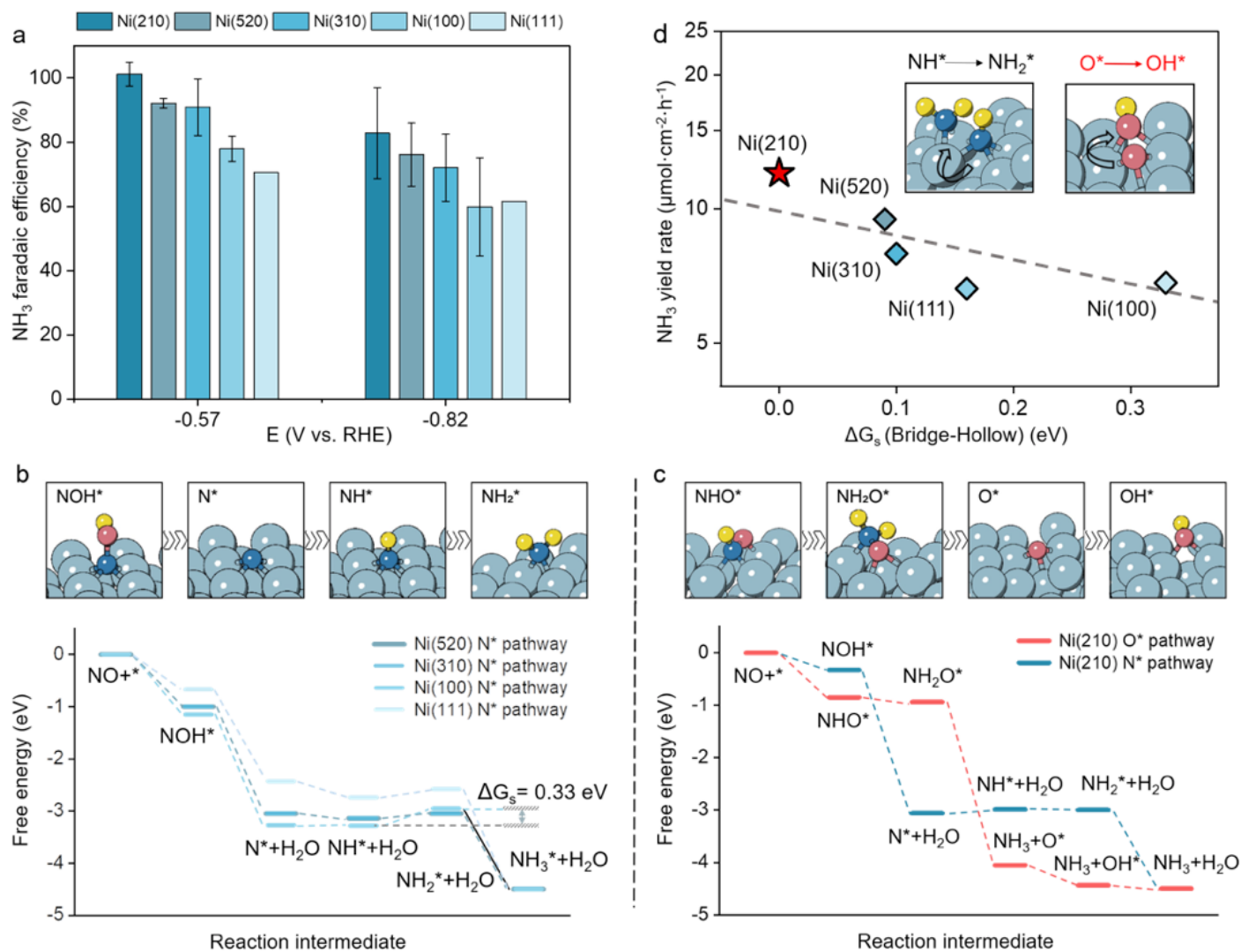


Figure 3

Mechanistic understanding of NO-to-NH₃ conversion on Ni. (a) FE of NH₃ on five single-crystal Ni facets under two different potentials. The error bars represent the standard deviation of triplicate measurements. (b) Calculated free energy diagrams of N* pathway on four Ni facets. (c) Calculated free energy diagrams of O* (red) and N* pathway (blue) on Ni(210). Insets of (b) and (c) show cartoon illustrations of key intermediates along N* and O* reaction pathways, respectively. (d) The correlation between NH₃ yield rate (in a log scale) and ΔG_s on various Ni facets. Ni, N, O, H are coded by light blue, deep blue, pink and yellow respectively. The insets schematically show the location switch from hollow to bridge site in both N* and O* reaction pathways.

Supplementary Files

This is a list of supplementary files associated with this preprint. [Click to download.](#)

- [SupplementaryMaterials.pdf](#)